7-29-2023

Functionalized GO nanoplatelets with folic acid as a novel material for boosting humidity sensing of chitosan/PVA nanocomposites for active food packaging

Mohamed Morsy
mohamed.morsy@bue.edu.eg

Surfaces and Interfaces 41 (2023) 103229

Contents lists available at ScienceDirect

Surfaces and Interfaces

journal homepage: www.sciencedirect.com/journal/surfaces-and-interfaces

Functionalized GO nanoplatelets with folic acid as a novel material for boosting humidity sensing of chitosan/PVA nanocomposites for active food packaging

Hesham Moustafa [a,b,*], Mohamed H. Hemida [c], Mohamed A. Shemis [d], Alain Dufresne [e], Mohamed Morsy [f,g]

[a] Department of Polymer Metrology & Technology, National Institute of Standards (NIS), Tersa Street, El Haram, P.O Box 136, Giza 12211, Egypt
[b] Bioanalysis Laboratory, National Institute of Standards (NIS), Tersa Street, El Haram, P.O Box 136, Giza 12211, Egypt
[c] Agricultural Engineering Department, Faculty of Agriculture, Cairo University, Giza, Egypt
[d] Department of Biochemistry and Molecular Biology, Theodore Bilharz Research Institute, Giza, Egypt
[e] Université Grenoble Alpes, CNRS, Grenoble INP, LGP2, Grenoble F-38000, France
[f] Building Physics and Environment Institute, Housing and Building National Research Center (HBRC), Dokki, Giza, Egypt
[g] Nanotechnology Research Center (NTRC), The British University in Egypt (BUE), El Sherouk City, Suez Desert Road, Cairo 11837, Egypt

ARTICLE INFO

Keywords:
Graphene oxide/folic acid humidity sensing material
Chitosan/PVA blend
Humidity sensor
Mechanical properties
Active food packaging

ABSTRACT

Humidity sensing materials play a pivotal role for serving as the essence of moisture sensors to trap surrounding water molecules through hydrophilic interaction, chemical bonding, or hydrogen bonds, therefore enhancing the sensor conductivity. Thus, this work addresses a highly efficient humidity sensing material based on folic acid (FA) functionalized graphene oxide (GO) which was prepared for consolidating inside chitosan (CS)/polyvinyl alcohol (PVA) (80/20) blend by the solvent casting approach. The structure of GO and its decoration were ratified by X-ray diffraction (XRD), Fourier transform infrared (FT-IR) and UV–vis spectroscopies. Three GO-FA contents (i.e., 10, 20, and 30 vol%) were utilized to fabricate the renewable CS/PVA nanosensors. The morphology of fabricated sensors was characterized by XRD and scanning electron microscopy (SEM). SEM images showed that the miscibility and dispersibility of GO-FA nanoplatelets in the CS/PVA matrix are better at 10 and 20 vol%, although the tensile strength increased to 69.40 MPa for the nanocomposite film containing 30 vol% GO-FA compared to the blank specimen. Moreover, other investigations such as Raman spectroscopy and antibacterial activities were performed on the CS/PVA sensors. The humidity sensing properties were carried out over a broad range of relative humidity from (7–97% RH) and frequency (100 Hz-100 kHz). The data revealed that 1 kHz was considered to be the optimum frequency. Furthermore, the obtained outcomes from humidity-sensing tests at 1 kHz showed that the sensor C10 had higher sensitivity with ultrafast response/recovery times (2.6 s/3.5 s) compared to other nanosensors, to be used in intelligent food packaging and preservation.

1. Introduction

Regarding the climate crisis and global warming, humid air or moisture is considered as a source of vexation and has a severe impact on other miscellaneous needful applications such as food products, pharmaceutical powders and tablets, agricultural crops, soil, and electronic devices [1–3], besides metrological measurements and biological products. Humidity generally impacts all forms of life, including humans, and is now a pressing concern worldwide [4]. Consequently, humidity control is crucial in such applications to reduce or prevent their risk of short-term damage. Humidity in terms of relative humidity (RH), which is defined as the amount of water vapor in the atmospheric envelope, must be detected even at trace levels by specific instruments [5,6]. Such instruments, humidity sensors are now becoming the first demand and focus of scholars for RH monitoring [7–9]. They should have unique properties such as fast response-recovery times, stability, high precision, and ability to connect effortlessly to equipment. These features open up the opportunities for their use in a variety of promising applications such as food packaging, medicine, agriculture, and environmental science. Sensors should generally be designed to be highly

* Corresponding author.
E-mail address: hesham.moustafa21@gmail.com (H. Moustafa).

https://doi.org/10.1016/j.surfin.2023.103229
Received 25 May 2023; Received in revised form 17 July 2023; Accepted 28 July 2023
Available online 29 July 2023

sensitive, fast response, low hysteresis, and cost effective [10,11]. To realize this, the humidity sensing substances must be developed according to these specifications. However, there is no humidity sensor that can meet all these requirements, thereby the choice of these varieties depends on the required application. Overall, humidity sensing substances must possess active sites to have fast response and recovery times [12]. However, these are necessary but insufficient conditions for achieving quality humidity sensors, especially in smart systems [13]. To achieve an optimal moisture sensor, the sensing material needs the aid of other reactive polar moieties such as hydrophilic or conducting polymers. For instance, humidity sensors in intelligent food packaging play a significant role for controlling food spoilage, because they can convey prompt information to the producer or consumer about shelf-life and expiration dates for consuming food products [14,15]. Efforts [16-19] have been extensively conducted to develop affordable sensing materials based on polymer-metal oxide nanocomposites to increase conductivity.

As known, moisture is a physicochemical phenomenon that requires a hydrophilic material (i.e. metal-oxide) to react and to trap surrounding water vapor molecules on its surface, therefore enhancing the sensitivity [2,13,20]. For this reason, folic acid functionalized graphene oxide (GO) was used in this work. 2D-GO nanoplatelets have been widely investigated for humidity and gas sensing, as well as semiconductor photocatalyst material because of their unique chemical structures with large specific surface area [21,22]. Their structure is like a honeycomb lattice consisting of carbon atoms and has reactive oxygenated groups such as epoxide ring, hydroxyl and carboxylic groups that act as hydrophilic sites to readily adsorb the water vaper molecules from the environment, thereby making the material highly electrically conductive [23–26]. Besides GO properties, folic acid (FA) is as well as hydrophilic material and has reactive sites such as carboxylic (-COOH) and amino (-NH_2, -NH) groups that can easily be functionalized with GO groups to create a highly efficient humidity-sensing material. Furthermore, it can also be combined with natural polysaccharides or synthetic biopolymers such as chitosan, PVA and others for boosting its use in a variety of applications such as cancer treatments [27,28], hydrogels for wound healing [29,30], biosensors [31], food packaging [32], and drug delivery [33].

Chitosan/PVA blends are considered to be a potential candidate for humidity sensors due to their biocompatibility and grafting with other biopolymers. Besides they present themselves as an excellent alternative to limit the environmental impact caused by petroleum-based-plastics. Moreover, CS/PVA blends are 100% biodegradable and non-toxic materials derived from renewable resources. For these advantages, recent studies reported that CS/PVA blend with glutaraldehyde as an interlocking agent used in tissue engineering applications [34,35]. In the sensor field, using nanoparticles (NPs) in humidity sensors could nevertheless overlook interlocking agents with these kinds of biopolymers, because NPs possess reactive groups that can react or link with them via hydrogen bonds to create a highly crosslinked matrix. NPs can impart high mechanical and antibacterial properties to these biopolymers, in addition to fast response/recovery times due to their chemical structures. To the best of our knowledge, no literature has used decorated GO/FA for humidity sensing purposes. Thus, the aim of the current work was to functionalize GO nanoplatelets by FA to boost humidity sensing properties of CS/PVA nanocomposites without requiring an interlocking agent. The GO/FA functionalization process was examined by XRD, FT-IR and UV–vis analysis. The native 2D-GO layered material was used for comparison. The CS/PVA nano-sensors fabricated by solvent casting route were then subjected to various tests such as morphology, Raman and mechanical investigations, as well as humidity sensing and antibacterial activity. The humidity sensing mechanism based on chemisorption and physisorption was also investigated. The obtained outcomes for these CS/PVA sensors revealed that they could be promising candidates for active-food packaging and other engineering applications.

2. Materials and experimental sections

2.1. Materials

Chitosan (CS) above 85% DA in powder form with a viscosity of 200–800 cP (1 wt.% in 1% acidic acid) [36] was supplied by Sigma-Aldrich, Cairo-Egypt. Polyvinyl alcohol (PVA) in powder form (~ 99% hydrolyzed, M_W ~ 115,000) was purchased from Oxford Laboratory, Mumbai-India. Graphene oxide (GO) nanolayered sheets used in this work were synthesized from graphite flakes by Hummer's approach as described previously [2]. Folic acid (FA, $C_{19}H_{19}N_7O_6$) in yellowish powder form with an assay $\geq$ 98% was provided by Alpha Chemika Co., Maharashtra-India. The chemical structure of prepared GO and its functionalization by FA were confirmed by different techniques as shown in Fig. 1. All other reagents and chemicals for controlling humidity levels were used as supplied without prior modification.

2.2. Synthesis of functionalized GO by FA

As presented in Fig. 1(a), the functionalization of synthesized GO by FA was performed by in situ hydrolysis as follows: 0.5 g of GO was dispersed in 100 mL deionized water (DIW) and sonicated using a probe Fisher Scientific Sonic Dismembrator, Model FB505, USA, for 15 min at 60% amplitude, keeping the dispersion in an ice bath to avoid solvent evaporation. Next, 0.4 g of FA was initially dissolved in a small amount of DIW and then added to the GO suspension. The mixing was followed by sonication for an additional 20 min. The sonicated mixture was then maintained under stirring conditions overnight to complete the chemical reaction. After that, a small amount of the mixture was dried under normal conditions to be investigated by XRD, FT-IR, and UV–vis irradiation. The other part was left to be incorporated into the CS/PVA blend. The samples were coded based on the concentration of GO-FA in the blend matrix as displayed in Table 1.

2.3. Fabrication of CS/PVA-GO-FA nanocomposite films

CS/PVA-GO-FA biofilms were obtained by film-forming dispersion as follows: 1 g of CS was dissolved in 100 mL of acidic solution (1 vol%) and stirred overnight to achieve the dissolution process. After that, the solution was filtered to eliminate any impurities and kept in a volumetric flask. On the other hand, 2.5 g of PVA powder was dissolved in 50 mL of DIW and stirred at 85 ºC for 120 min. Next, both biopolymers (CS/PVA) were mixed at a volume ratio (80:20) at room temperature for 30 min before adding the decorated GO-FA nanosheets. To fabricate the biofilms, three different concentrations (i.e., 10, 20 and 30 vol%) were utilized and individually added to the CS/PVA blend solution as specified in Table 1. Afterwards, the mixture was sonicated for a few minutes and kept under stirring conditions for 60 min in order to achieve a good dispersion of the decorated GO-FA into the CS/PVA blend. Lastly, the obtained mixture was poured onto a 90 mm diameter Teflon dish and left for 7 days at room temperature for solvent evaporation (Fig. 1(a)). After the drying process, the biofilms were pulled-off from the Teflon dishes and further dried in a laboratory oven at 60 ºC for 3 h The unfilled CS/PVA blend was fabricated under the same conditions for comparison. The prepared nanocomposite films were then labeled based on the GO-FA content in the CS/PVA matrix as presented in Table 1.

2.4. Characterization techniques

2.4.1. X-ray diffraction analysis

The structure and morphology of native GO and decorated GO-FA, as well as nanocomposite films were investigated using a Philips X-ray diffractometer (PW 1930 generator, PW 1820 goniometer, The Netherlands) equipped with Cu Kα radiation ($\lambda = 1.54$ Å, 45 kV and 40 mA). Data were scanned over a 2Θ range from 10 to 80° with step size of 0.05 and at a step counting time of 2 s/step for powder samples and of

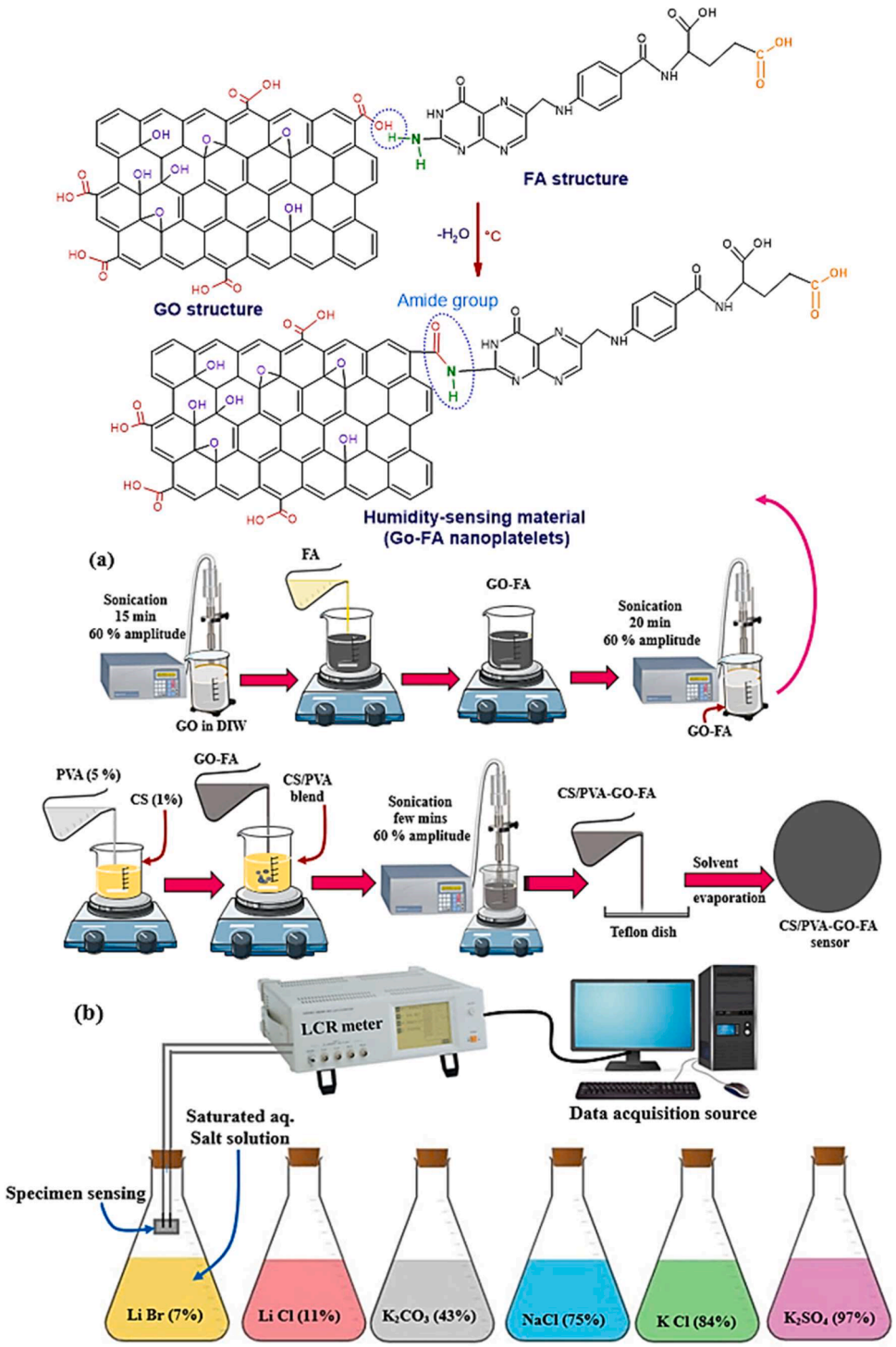

Fig. 1. (a) Schematic of the synthesis steps of GO-FA, CS/PVA-GO-FA sensors, and (b) Humidity-sensing tests for the fabricated sensors.

Table 1
Composition and codification of the fabricated nanocomposite films with different contents of functionalized GO-FA.

Sample	CS/PVA blend	CS/PVA-10 GO-FA	CS/PVA-20 GO-FA	CS/PVA-30 GO-FA
Film code	B	C10	C20	C30
CS/PVA (80/20) (v/v%)	100	90	80	70
GO-FA (v/v%)	0	10	20	30

0.013°/min for films, and at a sampling width of 0.010°.

2.4.2. Fourier transform infrared spectroscopy (FT-IR)

FT-IR spectra in transmission mode were performed to detect the chemical functionalization of FA with GO using a Thermo Scientific Nicolet model 380 Spectrometer, USA in the 4000–400 cm^{-1} spectral range. For nanocomposite films, FT-IR spectra with an imaging Spectroscope (FT-IR-IM) were implemented to study the chemical interactions between the components, as well as the topography of the prepared samples using a Bruker LUMOS II (Bruker, Hamburg, Germany). The FT-IR spectra were recorded with OPUS software, version

8.2, using the attenuated total reflection mode, in the spectral range 4000–600 cm^{-1} with a resolution of 4 cm^{-1} and 64 scans. Moreover, H_2O/CO_2 compensation was eliminated from each spectrum to overcome signals caused by environmental conditions between the 2400 cm^{-1} and 1850 cm^{-1} region.

2.4.3. UV–vis spectroscopy

The absorbance of synthesized GO nanosheets and their FA decoration was determined using a double beam UV–vis spectrophotometer from Shimadzu, Japan; model UV3101pc, over the wavelength range from 200 to 800 nm with a wavelength interval of 0.1 nm [37]. The prepared specimens were sonicated for a few minutes before testing to achieve homogeneity of the material.

2.4.4. Raman spectroscopy

Raman spectroscopy was implemented to explore the structural changes of cast sensor films and their chemical interactions using a Confocal Raman Microscope (Horiba LabRam HR Evolution Raman Spectrometer, France) with CapuR laser trapping at wavelength of 532 nm in the spectral range of 3000–80 cm^{-1}.

2.4.5. Mechanical properties

Tensile parameters in terms of tensile strength and strain at rupture for fabricated biofilms were tested using a Zwick (Germany) tensile testing machine (Model Z010) equipped with a load cell of 1 kN and a crosshead speed of 100 $mm.min^{-1}$, according to ASTM D 882–18. Dumbbell specimens were die-cut from the cast biofilms. Prior to testing, all specimens were conditioned at a temperature of 23 ± 2 °C and 50 ±5% RH for at least 24 h, which were monitored using a Hygrometer Testo, UK [38]. The average of five trials for each cast film was taken.

2.4.6. Humidity-sensing tests

The humidity sensors were evaluated over a wide range of relative humidity from 7% to 97% at room temperature (RT = 23 °C ± 2). The blank sensor was first evaluated under different testing frequencies from 100 Hz to 100 kHz under 1VAC to determine the optimal testing frequency, as illustrated in Fig. 5(a). The humidity sensing characteristics of the sensors were then evaluated under varying humidity levels using saturated salt solutions according to ASTM E 104–14 standard [39]. Saturated salt solutions of (LiBr, 99%), (LiCl, 97%), (K_2CO_3,99%,), (NaCl, 98%), (KCl, 97%), and (K_2SO_4, 99%) were offered from ADWIC Co., Cairo, Egypt and used to generate standard humidity levels of 7%, 11%, 23%, 43%, 75%, 84%, and 97%, respectively. To confirm the generated humidity level, a TSI 7415 hygrometer was used. The sensor was first let to stabilize at 7% and 97% RH for 5 h before starting the measurements. This has been done to obtain a reliable reading and reduce the signal-to-noise ratio. The impedance variation as a function of humidity for all sensors was performed using applied 1 VAC. Firstly, the humidity sensor was hung in a closed flask containing a saturated salt solution for 5 min, then the impedance value was recorded at different testing frequencies. The previous step was repeated for each humidity level. The impedance values were acquired using HIOKI-3532–50 LCR meter (Fig. 1(b)). The sensitivity, of all examined sensors, was evaluated in terms of impedance variation as a function of humidity level. For the repeatability, response and recovery time, the impedance was recorded as a function of time every 3 s.

2.4.7. Antibacterial assay

Staphylococcus aureus (ATCC 6538) and *Escherichia coli* (ATCC 8739) were used to represent G^{+ve} and G^{-ve} bacteria, respectively, in this work. The antibacterial activity evaluation procedure was performed using the agar disc diffusion route as previously described in the literature [36, 40].

3. Results and discussion

3.1. Characterization of synthesized GO and GO-FA

XRD, FT-IR and UV–vis analyses were used to investigate the synthesized GO and to confirm the functionalization process of GO by folic acid (FA), as illustrated in Fig. 2(a-c). The typical XRD pattern for prepared GO was given in Fig. 2(a) in which a sharp characteristic peak, indexed as the basal plane (d_{oo1}), appeared at ~ 2Θ= 11.97° with a D-spacing distance of ~ 7.39 Å [41] compared to 3.36 Å for graphite [42]. This increase in the interplatelet spacing (d-spacing) was correlated with the insertion of oxides groups such as hydroxyl, carboxylic and epoxy between the graphene sheets and at the edges as well, proving that chemical oxidation of graphene to GO was achieved. After functionalization of GO by FA, a shift of the GO diffraction peak towards lower 2Θ angles, from 11.97° to 9.45°, associated with an increase in the D-spacing distance from 7.39 Å to 9.36 Å was observed. This shift and the increase in the D-spacing distance indicate that FA molecules can penetrate between the stacked GO layers, leading to the expansion of the interlayer distance. This will enhance the penetration of polymer chains between GO nanosheets for obtaining GO intercalation/or exfoliation structure. Moreover, a slight leftward shift of few sharp diffraction peaks located at 2Θ of 10.80°, 13.02°, 26.7°, and 27.75°, compared to pure FA, was also noted and assigned to FA [43]. Additional characterization data for GO and decorated GO-FA were supported by FT-IR and UV–vis spectroscopies. As shown in Fig. 2(b), a broad peak located at the region of ~ 3450–3240 cm^{-1} was corresponded to the stretching of -OH and -NH groups [44]. It was also noticed that the peak position for -C = O in GO-FA was found to be slightly shifted to lower wavenumber (i.e., ~ 1689 cm^{-1}) compared to -COOH carboxylic group (i.e., 1715 cm^{-1}) in native GO nanoplatelets. This shift was attributed to the covalent bond formation of amide group (-CO—NH-) in GO-FA, confirming that the functionalization of GO by FA occurred (Fig. 1(a)). In addition, an increase in the absorption spectrum of GO-FA ranging from 315 to 375 nm was observed compared to native GO, as presented in Fig. 2(c).

On the other hand, Fig. 2(d) showed the XRD patterns for the blank and C10, C20, and C30 nanocomposites. The diffraction patterns of C10, C20, and C30 samples showed multiple diffraction peaks belonging to GO FA and CS/PVA. A broad signal can be seen centered around 2θ = 19.3° due to the presence of CS/PVA polymer matrix, indicating a highly amorphous structure for the blend matrix [45]. This implied that a chemical interaction between the functional groups from both polymers occurred, which affected the CS property against the bacteria as reported herein. However, the diffraction pattern of C10 sample exhibited less intense peaks, the characteristic peaks of GO and FA can be recognized. It was also observed from Fig. 2(d) that the intensity of GO peak, at 2θ = 10.9° (d-spacing = 9.5 A°) increased as the concentration of GO increased. The same observation was made for folic acid, where its concentrations also increased with increasing GO content. However, the diffraction peak at 2Θ= 10.9° disappeared when PVA was added to CS in the blend compared to CS itself [46]. Addition to this, some related structural parameters were calculated to get more information regarding the crystallite size (D), lattice strain (ε), inter-planar distance (d), dislocation density (δ), number of crystallite size per unit area (N) and distortion parameters (g) were studied using the following formula [47–49] and the data listed in Table 2.

$$D = \left[\frac{(k) \times (\lambda)}{(\beta_D) \times (\mathrm{Cos}\theta)}\right] \quad (1)$$

$$\varepsilon = \left\{\frac{\beta_D}{4 \times \sin\theta}\right\} \quad (2)$$

$$d = \frac{\lambda}{2\sin\theta} \quad (3)$$

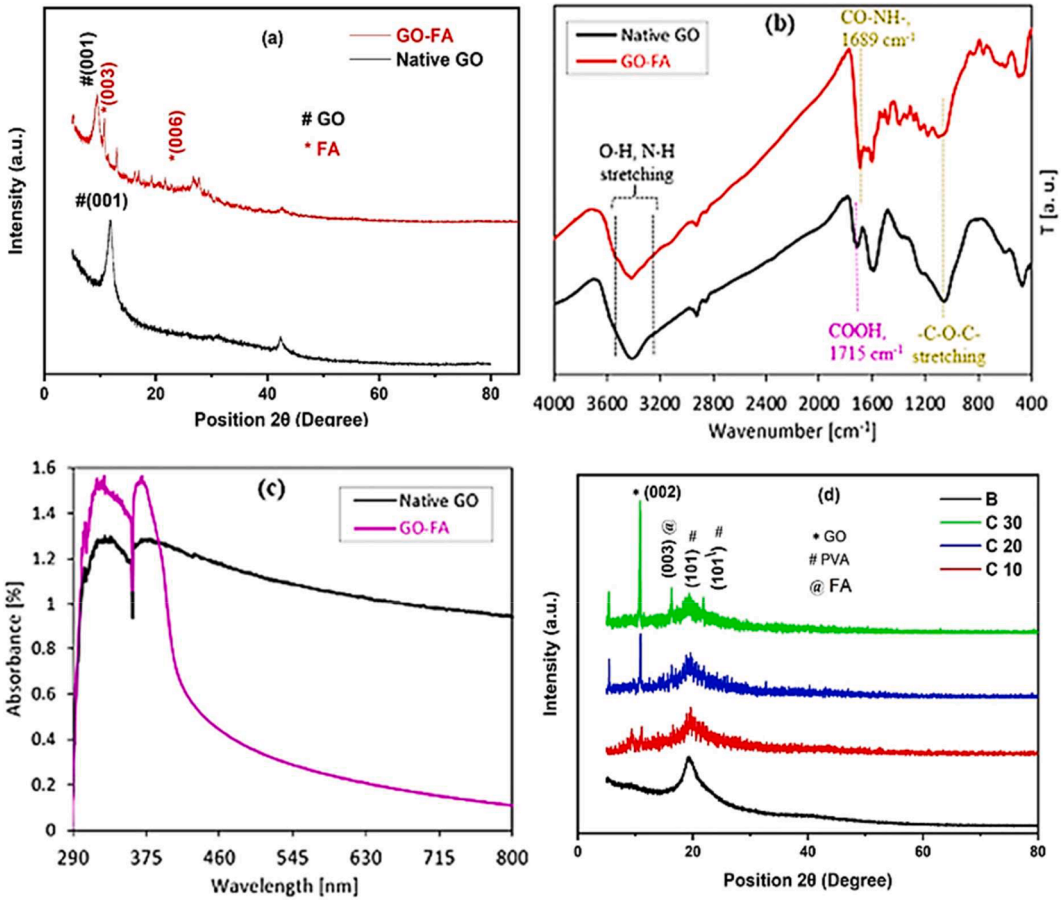

Fig. 2. (a) XRD patterns, (b) FT-IR spectra, (c) UV–vis spectra for GO and decorated GO-FA, and (d) XRD patterns for CS/PVA nanocomposites.

Table 2
XRD parameters of B, C10, C20, and C30 sample.

Sample	D (nm)	d-spacing (Å)	ε	δ (nm^{-2})	N	g
B	125.8939	0.901152	0.003221	6.31E-05	5.69E-05	0.012884
C10	39.87645	0.610148	0.006885	0.000629	0.000384	0.027542
C20	58.86498	0.610844	0.00467	0.000289	0.000176	0.018679
C30	73.85716	0.616348	0.003755	0.000183	0.000113	0.015021

$$\delta = \left\{\frac{1}{D^2}\right\} \quad (4)$$

$$N = \frac{d}{D^2} \quad (5)$$

$$g = \frac{\beta}{\tan\theta} \quad (6)$$

Where λ is the wavelength for x-ray source (CuK_α) and β represents the full width at the median of the highest value, θ is the diffraction angle.

The calculated XRD parameters of Table 2 demonstrated that the D-spacing and crystallite size increased as the amount of the GO-FA increases. On contrary the crystallite size per unit area decreased as the GO-FA proportion increases. This could be explained based on the increment of the crystallite size.

Fig. 3(a) showed the FT-IR-IM spectra for incorporated CS/PVA blend and its nanocomposites with varying ratios of GA-FA. The characteristic bands centered at 3247–3560 cm^{-1} assigned to -OH and -NH stretching vibrations and 1724 cm^{-1} (carbonyl group) for chitosan in CS/PVA blend matrix. However, the latter band was absent in the case of C10 and started to become an apparent band at ~ 1685 cm^{-1} in the case of C20 and C30 samples. It shifted to lower wavelengths, indicating that the chemical reaction between carboxylic acid group in FA and amino group in CS took place and amide group formed. Meanwhile, the intensity of the bands at ~3560–3247 cm^{-1} was reduced with increasing GO-FA concentration to 30 vol% in the CS/PVA matrix. The cause for this may be due to hydrogen bond conjugations between functional sites such as -OH, N—H and -C-H in the blend matrix, thereby overlapping in the same spectrum region [50]. All of these contributed to the miscibility and distribution of GO-FA nanosheets in the blend matrix, therefore promoting the tensile properties.

Additional data on the structural and chemical interactions between the CS/PVA blend and the decorated GO-FA were confirmed by Raman spectroscopy, as depicted in Fig. 3(b). The figure clearly showed the presence of two sharp peaks located at 1573 cm^{-1} and 1346 cm^{-1} in the Raman spectrum, which are ascribed to the G (sp^2 C atoms) and D (sp^3 C atoms) bands of synthesized pure GO, respectively [2,51]. These peaks appeared in highest intensities because of the conjugated and carbon-carbon double bonds of GO [42]. However, the G band of GO-FA in CS/PVA matrix is observed at 1598 cm^{-1}, which is slightly shifted from its position for native GO. Meanwhile, the intensities of these peaks

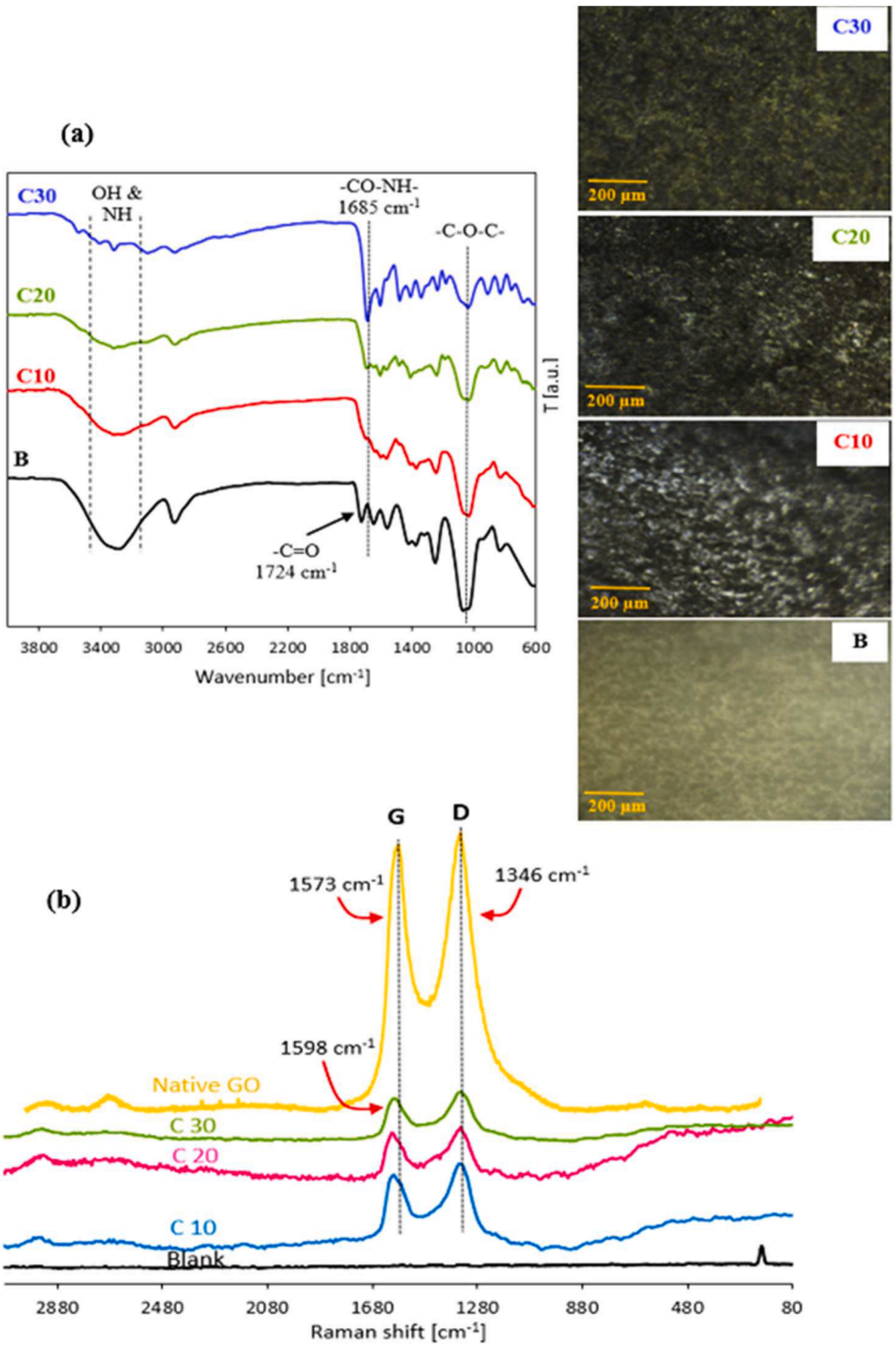

Fig 3. (a) FT-IR-IM imaging spectroscopy for CS/PVA blend and the nanocomposites, (b) Raman spectra for native GO, CS/PVA blend, and their nanocomposites.

were obviously reduced when GO material was incorporated into the polymer matrix. All of them indicate that chemical interactions between the oxygenated functional groups in GO-FA and CS/PVA blend were achieved. These outcomes are consistent with that verified elsewhere for CS/PVA/GO composite nanofibers [52]. Surprisingly, it was also noticed that the G and D intensities decreased when increasing the GO-FA concentration up to 30 vol% in the polymer blend, confirming the existence of more interfacial bonds. The achievement of chemical interactions between the components would contribute to the biocompatibility and dispersibility of GO-FA within the blend matrix to create new high-performance materials for end use products. This outcome agrees with that obtained from tensile properties and SEM observations.

3.2. SEM analysis

SEM observation can offer helpful information about the surface

morphology and dispersibility of GO-FA inside the biodegradable CS/PVA matrix. Fig. 4 displayed SEM micrographs of the fractured surface for CS/PVA nanocomposites reinforced with different proportions of GO-FA nanoplatelets. As depicted in Fig. 4(A), the pristine sample exhibited a smooth surface without any forging materials confirming the homogeneity of the cast film. For C10 and C20 samples, the GO-FA nanoplatelets seemed to be uniformly dispersed within the polymer matrix. As the concentration of GO-FA nanoplatelets increased to 30 vol %, the roughness of the film increases. More importantly, the surface of the C30 cast film appeared wrinkled. In spite of the distribution of GO-FA nanoplatelets, the sample exhibited some discontinuity in its internal structure.

3.3. Mechanical properties

Tensile tests performed on the fabricated nanocomposite films provide access to their tensile strength (T.S) and strain at rupture and allow exploring the impact of adding varying proportions of GO-FA to the of biodegradable CS/PVA nanocomposite films without requiring an interlocking agent. The results were presented in Fig. 5 and Table 3. The neat blend exhibited quite high tensile strength (~ 38 MPa) and strain at rupture (~ 39%). This outcome was almost consistent with that studied elsewhere [53]. Nevertheless, with the addition of GO-FA nanosheets to the CS/PVA blend, the tensile strength values increased dramatically when increasing the GO-FA nanosheet content. This increment in tensile strength values was ~ 25, 53, 81% for C10, C20, and C30 nanocomposites, respectively, compared to the neat blend. The reason for the improvement in these properties was most probably due to the strong chemical interactions between the decorated GO-FA nanosheets and CS/PVA blend. This, in turn, leads to the possibility of crosslinking through the interfacial bonding between the functional sites of GO-FA and the polymer blend. This evidenced that an effective stress transfer (i.e., better interfacial adhesion) between the nanofiller and the matrix was achieved [54,38]. Therefore, the tensile properties agree with those obtained by FT-IR analysis and SEM observations. On the other hand, it was noticed that the strain at break values reduced when adding GO-FA nanosheets at any proportion compared to the CS/PVA blend. This was due to the fact that the nanocomposite films became more compact after CS/PVA crosslinking by adding GO-FA. Similar results have been reported elsewhere [33], when adding genipin as crosslinking agent to PVA/Chitosan blend film.

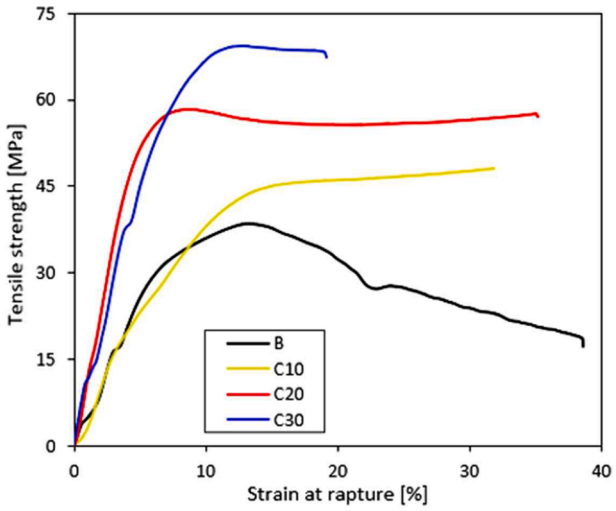

Fig. 5. Mechanical properties for CS/PVA blend and the nanocomposite films containing varying amounts of GO-FA nanoplatelets.

Table 3
Tensile parameters for fabricated CS/PVA nanocomposites.

Sample code	B	C10	C20	C30
T.S at max (MPa)	38.40±0.66	48.02±0.38	58.45±0.29	69.40±0.65
S. B (%)*	38.70±5.86	32.36±7.15	35.54±5.24	19.42±6.37

* S. B (%): Strain at break.

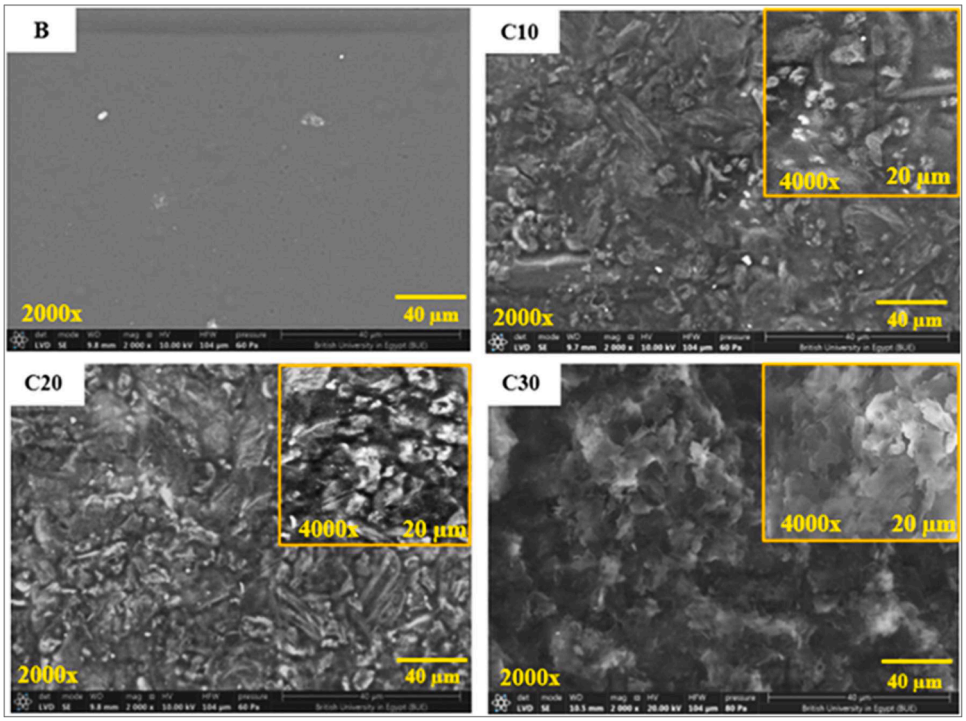

Fig. 4. SEM images for CS/PVA blend and the nanocomposites with different proportions of decorated GO-FA at different magnifications (i.e., 2000x and 4000x).

3.4. Humidity sensor assessment

The cast humidity sensors were tested under different humidity levels at room temperature using saturated salt solutions. The blank sample was measured at different testing frequencies of 100 Hz, 1 kHz, 10 kHz, and 100 kHz as illustrated in Fig. 6(a). It was found that as the testing frequency increases, the slope of the impedance curve decreases, confirming the effect of testing frequency on the response of the tested sensor. This behavior might be related to the polarizability of water molecules. As the frequency increased, the water molecules cannot follow the rapid alternation of the applied signal, causing the impedance variation to decrease [55–57]. Although, the highest variation value was achieved at 100 Hz, subsequent evaluations for other sensors were performed at 1 kHz due to the linearity of the measured values. The variation of impedance as a function of humidity level for all tested sensors at 1 kHz is depicted in (Fig. 6(b)). The sensitivity (S) of all sensors was calculated using the following equation [56]:

$$S = \frac{Z_7 - Z_H}{RH_H - RH_7} \quad (7)$$

Where Z_7 and Z_H represent the impedance value at 7% humidity level (RH_7) and high humidity level (RH_H), respectively. The calculated sensitivity for B, C10, C20, and C30 sensor samples were found to be 0.23 MΩ/RH, 0.49 MΩ/RH, 0.39 MΩ/RH, and 0.47 MΩ/RH, respectively. The highest sensitivity was attained for the C10 sample compared to C20 and C30 sensor samples as shown in bar graph of Fig. 6(c). The reason would apparently be attributed to the increase of active sites in the matrix with the addition of GO-FA nanosheets, leading to the increase of the resulting nanocomposite surface area [2]. However, when further increasing the GO-FA concentration to 20 or 30 vol%, more hydrogen bonds were formed within the matrix rather than reacting with external humid air, therefore decreasing the sensor sensitivity. These outcomes were supported by FT-IR analysis.

Complex impedance spectroscopy (CIS) is one of the most valuable techniques for evaluating the humidity sensing mechanism. The CIS curves were measured from 50 Hz to 5 M Hz under different humidity levels as shown in Fig. 6(d). As evidenced from Fig. 6(c), the CIS curves have different shapes depending on the humidity level. The sensing mechanism can be divided into three main stages, including low, medium and high humidity. The sensing mechanism can be explained by visualizing adsorbed water molecules as sequential layers (Fig. 7(a)). At low humidity level, a double hydrogen bond (chemical bond) was created between adsorbed water molecules and the sensor surface, thereby the charge carriers were restricted in their locations. The straight line at this low humidity level represented the intrinsic impedance property of the sensor. At this stage, the hydroxyl groups are generated due to the interaction between adsorbed water molecules and active sites of sensing materials, as expressed by Eq. (8). As humidity increases, a second layer of water molecule was physically adsorbed onto the chemically adsorbed layer. In the medium humidity range, the generated hydroxyl groups (OH^-) interacted with the physically adsorbed water layer to generate hydronium ions (H_3O^+) which can be expressed by Eq. (9). At high humidity range, the generated hydronium ions can interact with the adsorbed water layers, thereby more hydronium ions were generated and move freely between adjacent water molecules (Grotthus chain reaction):

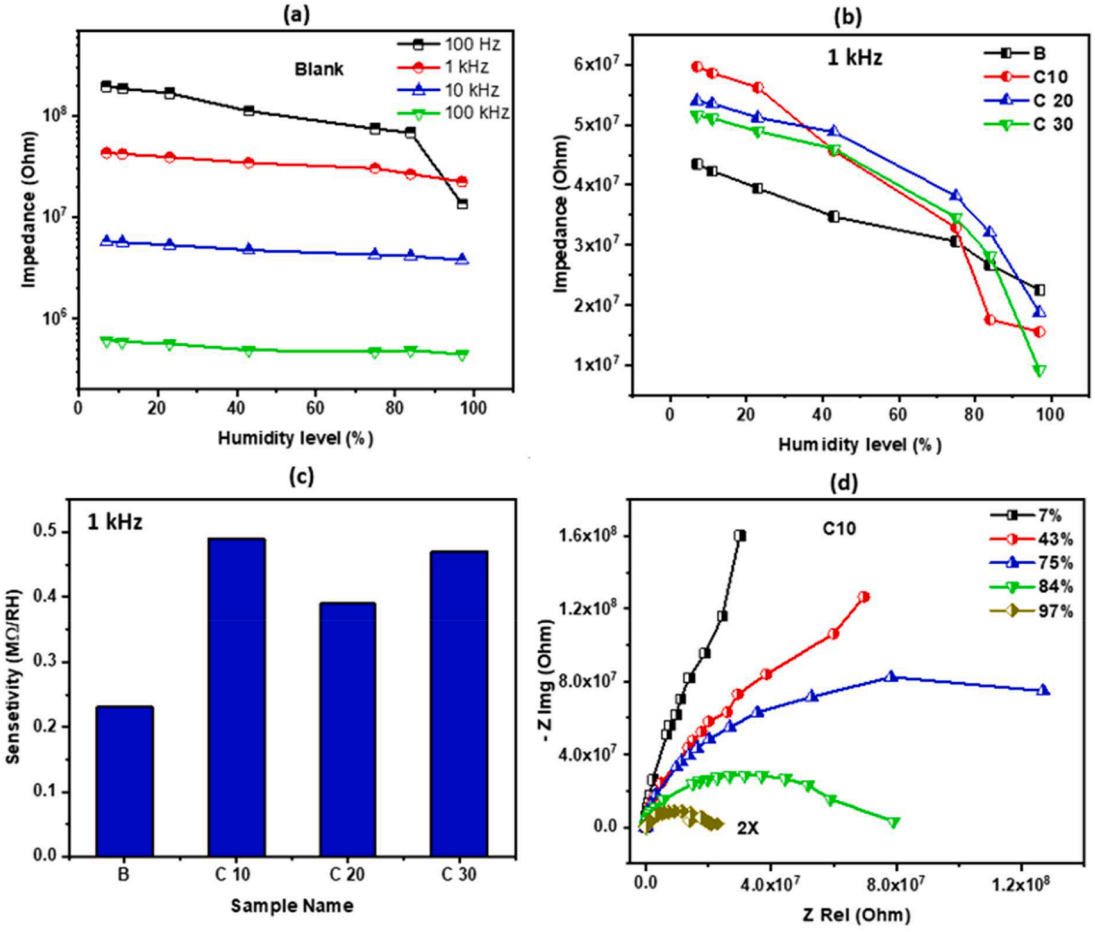

Fig. 6. (a) Humidity sensing tests for blank sample at different testing frequencies, (b) All sensors tested at 1 kHz, (c) Sensors sensitivity tested at 1 kHz, and (d) Complex impedance spectroscopy curves for C10 sensor at different humidity levels.

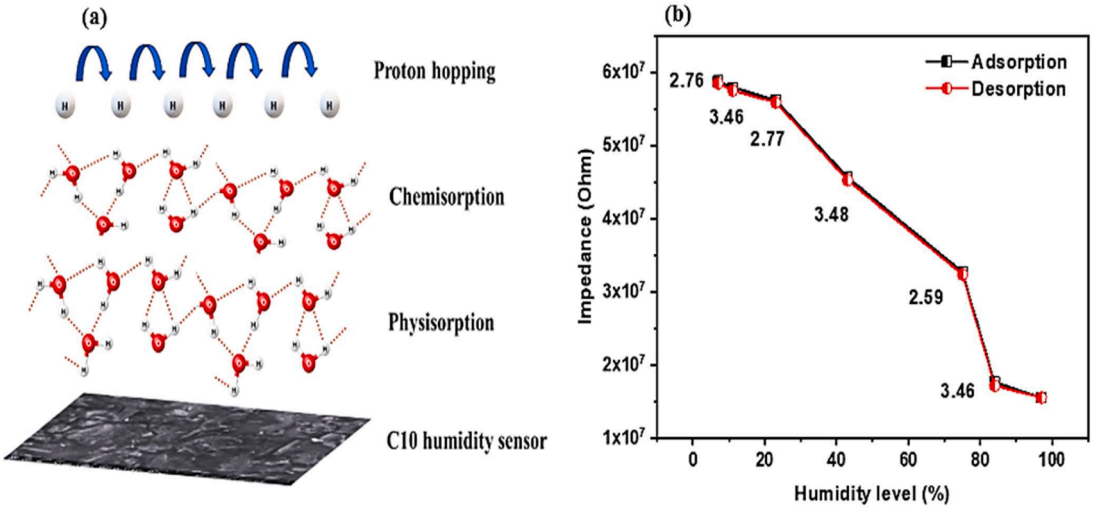

Fig. 7. (a) The proposed humidity sensing mechanism, (b) The hysteresis effects of C 10 sample due to the adsorption and desorption of water molecules.

$$H_2O \rightarrow H^+ + OH^- \quad (8)$$

$$H_2O + H^+ \rightarrow H_3O^+ \quad (9)$$

$$H_3O^+ + H_2O \rightarrow H_3O^+ + H_2O \quad (10)$$

Hysteresis is one of the most important parameters that describes the adsorption and desorption of water molecules during the humidification and dissociation process [58,59]. The maximum hysteresis (H) was calculated using the following equation [60]:

$$H = \frac{Z_D - Z_A}{S} \quad (11)$$

Where, Z_D and Z_A represents the impedance during desorption and adsorption process, while S is the sensitivity. The lowest the hysteresis the good practice for humidity sensor. The hysteresis behavior of C10 sample was displayed in Fig. 7. It can be observed that the C10 sample demonstrates a lowest hysteresis that favor its utilization in humidity sensing applications.

3.4.1. *Response/recovery characteristics for C10 sensor*

The response and recovery characteristics of the C10 sensor were evaluated for three cycles as presented in Fig. 8(a). The C10 sensor was subjected to two humidity levels (7% and 75%RH) for 5 min each. The real time response as a function of impedance was recorded every three seconds. As shown in the figure, the C10 sensor responds instantly to humidity and then quickly returns to the base line value (7%). On the other hand, the speed of the sensor's response to external stimuli can be assessed by measuring its response time and recovery time. Response/recovery times can be defined as the time required by the sensor to reach 90% of its maximum value [61]. The calculated response and recovery times for C10 sensor are 2.6 s and 3.5 s, respectively, as showcased in Fig. 8(b). It can be seen that the sensor responds instantly humidity fluctuations, which could be due to the presence of abundant active terminal function groups, such as hydroxyl, amino, and carboxylic groups, of GO-FA that easily trap water vapor molecules from the atmosphere [2]. Thereby, the sensor responded very well to electricity. Further, Table 4 epitomizes humidity sensing properties of GO/FA material consolidated inside CS/PVA matrix and other humidity-sensing materials explained in previous literature. The comparative outcomes highlighted that the fabricated C10 sensor illustrated rapid response/recovery times than the other comparable humidity sensors regardless the sensor composition and the fabrication methods.

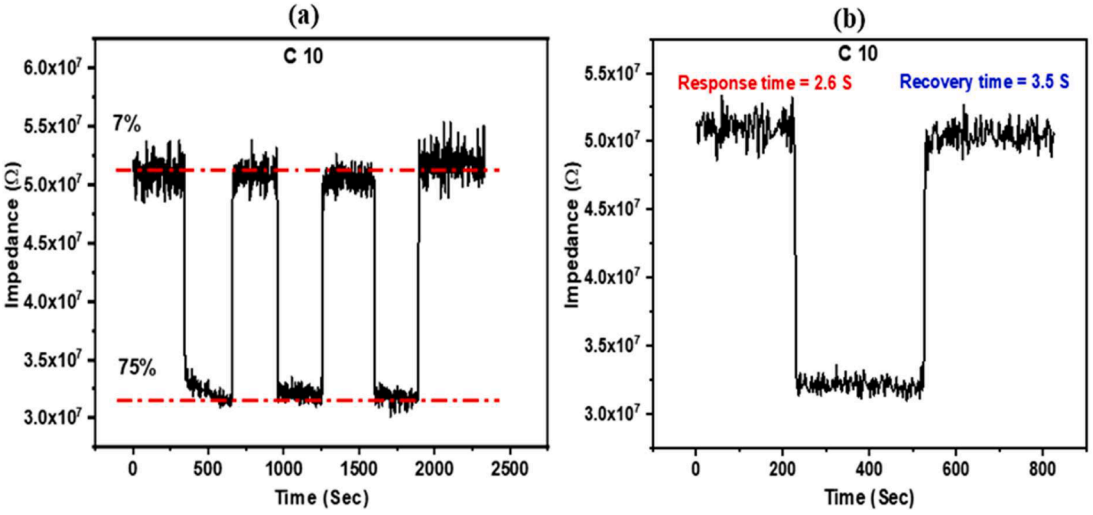

Fig. 8. (a) The repeatability of the C10 sensor, and (b) Response/recovery times of the C10 sensor.

Table 4
Humidity sensing properties compared to other researches.

Sensing materials	Fabrication method	Measurement range (%)	Sensitivity	Response/ recovery time (s)	Ref.
Titania nanorods/rGO	Hydrothermal	11 −97	N/A	40/160	[62]
Graphene/carbon ink	Screen printing	25–91.7	12.4 Ω/%RH	4.0/6.0	[63]
GO-$Zn_{1-x}Mn_xO$	Sol-gel	10–90	N/A	4.5/21	[64]
PDDA/rGO	LbL Self-assembly	11–97	N/A	108/94	[65]
CS/PVA	Spin coating	21–89	N/A	N/A	[66]
PVA/NC/$MgCl_2$	Solution casting	11–98	9.2 mV/% RH	6/11	[67]
PVA/GF	Spin coating/spray coating	40–90	29 nF/%RH	2./3.2	[68]
PVA/PANI/clay	Casting	11–97	0.0914 k/ RH	6/10	[69]
GO/Folic acid	Casting	7–97	0.49 MΩ\RH	2.5/3.6	This work

3.5. Antibacterial activity

Fig. 9 showed the in vitro antibacterial activity of the bio-nanocomposites which was determined by agar disc diffusion assay and the inhibitory zones are listed in Table 5. A clear inhibition zone was only observed around the discs for CS/PVA blend filled with decorated GO-FA, even at all investigated concentrations. However, a smaller inhibitory zone appeared for the control for both bacteria. The reason was probably due to the fact that the PVA added to CS can react with the functional sites of CS, thereby hindering its activity to kill bacteria. This finding agrees with that obtained by XRD data. In contrast, the inhibitory effects of the biologically synthesized filled biofilms were observed at different concentrations of 10,20 and 30 vol% GO-FA against *S. aureus* and *E. coli*. The bactericidal activity of the nanocomposite films showed that the inhibition zone increased when increasing the concentration of decorated GO-FA in the matrix depending on the type of bacteria as depicted in Fig. 9 and Table 4. This result might be ascribed to the insertion of GO-FA reacting with PVA rather than CS, besides the formation of amide groups (CO—NH) (i.e., acting as antimicrobial peptide group) between CS and GO-FA (Fig. 1(a)), which are efficiently strong in suppressing the spread of a wide range of G^{+ve} *bacteria* and G^{-ve} *bacteria* towards interrupting pathogen developments [70,71].

Table 5
Inhibitory zones for B, C10, C20, and C30 nanocomposite films against *S. aureus* and *E. coli* bacteria.

Pathogenic strains	Inhibitory Zone (mm)			
	B	C10	C20	C30
S. aureus	2.0 ± 0.10	17±0.15	19±0.27	23±0.18
E. coli	3.0 ± 0.13	16±0.38	20±0.23	25±0.46

4. Conclusions

In this manuscript, a novel humidity sensing material based on the functionalization of synthesized GO by FA was successfully prepared via *in-situ* hydrolysis. The chemical structure of GO and decorated GO-FA nanoplatelets was proved by XRD, FT-IR and UV–vis spectroscopy. Flexible humidity sensors were then fabricated by consolidating the decorated GO-FA nanoplatelets in the CS/PVA blend for boosting the mechanical and humidity sensing properties compared to those fabricated by spray coating or casting approaches. Three concentrations of GO-FA (i.e., 10, 20, and 30 vol%) were used to prepare the sustainable humidity sensors. XRD and FT-IR evidenced that chemical interactions between the CS/PVA matrix and GO-FA were achieved. SEM images showed good miscibility and dispersibility of GO-FA within the matrix, especially for sensors C10 and C20. The tensile strength of the fabricated sensors was augmented nearly twice in case of C30 sensor (i.e. ~ 70 MPa) that of the neat blend (i.e. ~ 38 MPa) when 30 vol% GO-FA used. Also, CS/PVA nanocomposites-based GO-FA displayed strong antibacterial properties against G^{+ve} bacteria and G^{-ve} bacteria as compared to the blank specimen. Furthermore, the humidity sensing test was performed by exposing the sensors to different levels of relative humidity ranging from 7% to 97% RH at 1 kHz. The obtained outcomes revealed that the sensitivity of the C10 sensor increased rapidly with the humidity level compared to other sensors. Furthermore, the response and recovery times for the C10 sensor were determined to be 2.6 s and 3.5 s, respectively. This enhancement was attributed to the oxygenated and aminated sites in both GO-FA and CS/PVA polymer that allow extra water vapor molecules to be adsorbed, and thus boosting the response. These outcomes confer the prepared humidity sensors many features

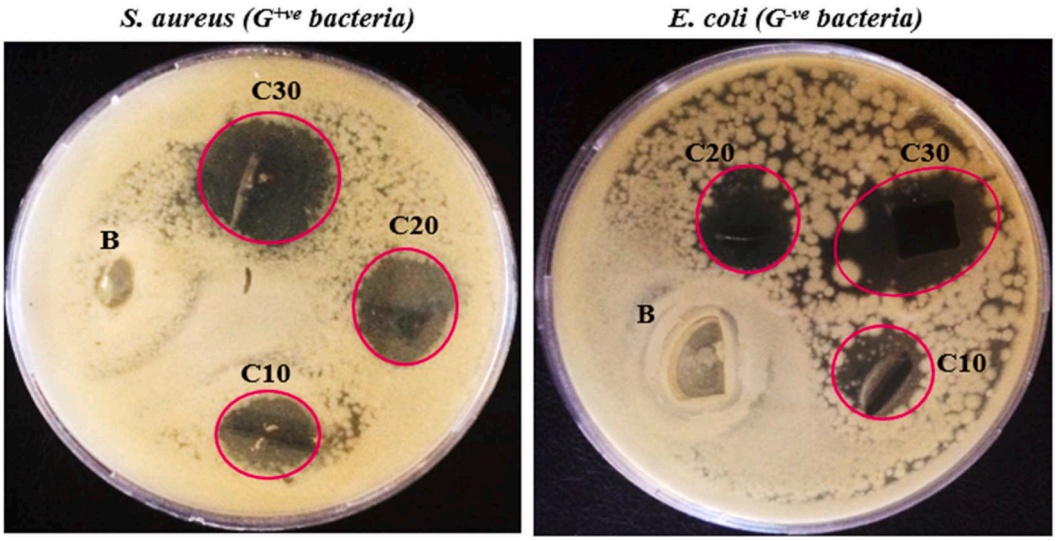

Fig. 9. Antibacterial activity of B, C10, C20, and C30 nanocomposite films against *S. aureus* and *E. coli* bacteria.

such as higher sensitivity, repeatability, low hysteresis, cost-effectiveness, and ultrafast response/recovery times. Therefore, this work reveals that these sustainable sensors can serve as RH sensors for promising applications such as smart food packaging and other prospective applications.

Credit author statement

Hesham Moustafa: Conceived the idea, Preparation, Writing-Reviewing and Editing the final manuscript. **Mohamed H. Hemida:** Experimentation and Data collection **Mohamed A. Shemis:** Visualization and Investigation. **Alain Dufresne:** Contributed in the writing-Reviewing and Editing the final manuscript. **Mohamed Morsy**: Experimentation and contribution in writing-original draft preparation. All authors read and approved the final manuscript.

Declaration of Competing Interest

The authors declare that there is no conflict of interest in this study

Data availability

The data that has been used is confidential.

References

[1] B. Arman Kuzubasoglu, Recent studies on the humidity sensor: a mini review, ACS Appl. Electron. Mater. (2022), https://doi.org/10.1021/acsaelm.2c00721.

[2] H. Moustafa, M. Morsy, M.A. Ateia, F.M. Abdel-Haleem, Ultrafast response humidity sensors based on polyvinyl chloride/graphene oxide nanocomposites for intelligent food packaging, Sensors Actuators A Phys. 331 (2021), 112918, https://doi.org/10.1016/j.sna.2021.112918.

[3] Z. Ma, T. Fei, T. Zhang, An overview: sensors for low humidity detection, Sensors Actuators B Chem. 376 (2023), 133039, https://doi.org/10.1016/j.snb.2022.133039.

[4] K.P. Ferentinos, N. Katsoulas, A. Tzounis, T. Bartzanas, C. Kittas, Wireless sensor networks for greenhouse climate and plant condition assessment, Biosyst. Eng. 153 (2017) 70–81, https://doi.org/10.1016/j.biosystemseng.2016.11.005.

[5] H. Farahani, R. Wagiran, M.N. Hamidon, Humidity sensors principle, mechanism, and fabrication technologies: a comprehensive review, 2014. doi:10.3390/s140507881.

[6] C.Y. Lee, G. Bin Lee, Humidity sensors: a review, Sens. Lett. 3 (2005) 1–15, https://doi.org/10.1166/sl.2005.001.

[7] B. Chethan, H.G.R. Prakash, Y.T. Ravikiran, S.C. Vijayakumari, S. Thomas, Sensors and Actuators B : chemical Polypyyrole based core-shell structured composite based humidity Sensor operable at room temperature, Sensors Actuators B. Chem. 296 (2019), 126639, https://doi.org/10.1016/j.snb.2019.126639.

[8] B. Chethan, H.G.R. Prakash, Y.T. Ravikiran, S.C.V. Kumari, S. Manjunatha, S. Thomas, Talanta Humidity sensing performance of hybrid nanorods of polyaniline-Yttrium oxide composite prepared by mechanical mixing method, Talanta 215 (2020), 120906, https://doi.org/10.1016/j.talanta.2020.120906.

[9] S. Pratibha, B. Chethan, Y.T. Ravikiran, N. Dhananjaya, V.J. Angadi, Sensors and actuators A : physical enhanced humidity sensing performance of samarium doped lanthanum aluminate at room temperature, Sensors Actuators A. Phys. 304 (2020), 111903, https://doi.org/10.1016/j.sna.2020.111903.

[10] W. De Lin, H.M. Chang, R.J. Wu, Applied novel sensing material graphene/polypyrrole for humidity sensor, Sensors Actuators, B Chem. 181 (2013) 326–331, https://doi.org/10.1016/j.snb.2013.02.017.

[11] Y.T. Ravikiran, B. Chethan, Humidity sensing studies on conducting polymers: polyaniline and polypyrrole, Inorg. Chem. Commun. 145 (2022), 110019, https://doi.org/10.1016/j.inoche.2022.110019.

[12] P. Qi, Z. Xu, T. Zhou, T. Zhang, H. Zhao, Study on a quartz crystal microbalance sensor based on chitosan-functionalized mesoporous silica for humidity detection, J. Colloid Interface Sci. 583 (2021) 340–350, https://doi.org/10.1016/j.jcis.2020.09.029.

[13] M.P. Rupashree, K. Soppin, S. Pratibha, B. Chethan, Cost effective photocatalytic and humidity sensing performance of green tea mediated copper oxide nanoparticles, Inorg. Chem. Commun. 134 (2021), 108974, https://doi.org/10.1016/j.inoche.2021.108974.

[14] H. Moustafa, A.M. Youssef, N.A. Darwish, A.I. Abou-Kandil, Eco-friendly polymer composites for green packaging: future vision and challenges, Compos. Part B Eng. 172 (2019) 16–25, https://doi.org/10.1016/j.compositesb.2019.05.048.

[15] B. Fu, Q. Liu, M. Liu, X. Chen, H. Lin, Z. Zheng, J. Zhu, C. Dai, X. Dong, D.P. Yang, Carbon dots enhanced gelatin/chitosan bio-nanocomposite packaging film for perishable foods, Chinese Chem. Lett. 33 (2022) 4577–4582, https://doi.org/10.1016/j.cclet.2022.03.048.

[16] S. yeon Lee, I. bok Lee, U. hyeon Yeo, R. woo Kim, J. gyu Kim, Optimal sensor placement for monitoring and controlling greenhouse internal environments, Biosyst. Eng. 188 (2019) 190–206, https://doi.org/10.1016/j.biosystemseng.2019.10.005.

[17] L. Guo, H.B. Jiang, R.Q. Shao, Y.L. Zhang, S.Y. Xie, J.N. Wang, X. Bin Li, F. Jiang, Q.D. Chen, T. Zhang, H.B. Sun, Two-beam-laser interference mediated reduction, patterning and nanostructuring of graphene oxide for the production of a flexible humidity sensing device, Carbon N. Y. 50 (2012) 1667–1673, https://doi.org/10.1016/j.carbon.2011.12.011.

[18] A. Allahbakhsh, PVC/rice straw/SDBS-modified graphene oxide sustainable Nanocomposites: melt mixing process and electrical insulation characteristics, Compos. Part A Appl. Sci. Manuf. 134 (2020), 105902, https://doi.org/10.1016/j.compositesa.2020.105902.

[19] D. Zhang, D. Wang, X. Zong, G. Dong, Y. Zhang, High-performance QCM humidity sensor based on graphene oxide/tin oxide/polyaniline ternary nanocomposite prepared by in-situ oxidative polymerization method, Sensors Actuators, B Chem. 262 (2018) 531–541, https://doi.org/10.1016/j.snb.2018.02.012.

[20] K. Iqbal, M. Ahmad, A. Ahmad, M. Danish, T. Zeeshan, W. Tahir, A. Aslam, M. Amami, J. Abdelhak, Fabrication and characterizations of hybrid materials based on polyaniline, metal oxide, and graphene nano-platelets for supercapacitor electrodes, Inorg. Chem. Commun. 137 (2022), 109201, https://doi.org/10.1016/j.inoche.2022.109201.

[21] M. Al Kausor, D. Chakrabortty, Graphene oxide based semiconductor photocatalysts for degradation of organic dye in waste water: a review on fabrication, performance enhancement and challenges, Inorg. Chem. Commun. 129 (2021), 108630, https://doi.org/10.1016/j.inoche.2021.108630.

[22] F.S. Mirza, Z.E.H. Aftab, M.D. Ali, A. Aftab, T. Anjum, H. Rafiq, G. Li, Green synthesis and application of GO nanoparticles to augment growth parameters and yield in mungbean (Vigna radiata L.), Front. Plant Sci. 13 (2022) 1–19, https://doi.org/10.3389/fpls.2022.1040037.

[23] R. Alrammouz, J. Podlecki, A. Vena, R. Garcia, P. Abboud, R. Habchi, B. Sorli, Highly porous and flexible capacitive humidity sensor based on self-assembled graphene oxide sheets on a paper substrate, Sensors Actuators, B Chem. 298 (2019), 126892, https://doi.org/10.1016/j.snb.2019.126892.

[24] F. Majid, M.D. Ali, S. Ata, I. Bibi, A. Malik, A. Ali, N. Alwadai, H. Albalawi, M. Shoaib, S.A. Bukhari, M. Iqbal, Fe 3 O 4 /graphene oxide/Fe 4 [Fe (CN) 6] 3 nanocomposite for high performance electromagnetic interference shielding, 47 (2021) 11587–11595.

[25] M.D. Ali, A. Aslam, T. Zeeshan, R. Mubaraka, S.A. Bukhari, M. Shoaib, M. Amami, I. ben Farhat, S. ben Ahmed, J. Abdelhak, S. Waseem, Robust effectiveness behavior of synthesized cobalt doped Prussian blue graphene oxide ferrite against EMI shielding, Inorg. Chem. Commun. 137 (2022), 109204, https://doi.org/10.1016/j.inoche.2022.109204.

[26] M.D. Ali, F. Majid, A. Aslam, A. Malik, I. Wahid, S. Dildar, S. Waseem, A. Dahshan, Dielectric and electrical properties of synthesized PBGO/Fe3O4 nanocomposite, Ceram. Int. 47 (2021) 26224–26232, https://doi.org/10.1016/j.ceramint.2021.06.030.

[27] K. Hayashi, M. Moriya, W. Sakamoto, T. Yogo, Chemoselective synthesis of folic acid-functionalized magnetite nanoparticles via click chemistry for magnetic hyperthermia, Chem. Mater. 21 (2009) 1318–1325, https://doi.org/10.1021/cm803113e.

[28] X.C. Qin, Z.Y. Guo, Z.M. Liu, W. Zhang, M.M. Wan, B.W. Yang, Folic acid-conjugated graphene oxide for cancer targeted chemo-photothermal therapy, J. Photochem. Photobiol. B Biol. 120 (2013) 156–162, https://doi.org/10.1016/j.jphotobiol.2012.12.005.

[29] K. Kalantari, E. Mostafavi, B. Saleh, P. Soltantabar, T.J. Webster, Chitosan/PVA hydrogels incorporated with green synthesized cerium oxide nanoparticles for wound healing applications, Eur. Polym. J. 134 (2020), 109853, https://doi.org/10.1016/j.eurpolymj.2020.109853.

[30] H. Moustafa, H.E. Nasr, A.M. Youssef, Development of antibacterial carboxymethyl cellulose/quaternized starch bionanocomposites based on cinnamon essential oil nanoemulsion for wound healing applications, Biomass Convers. Biorefinery. (2022), https://doi.org/10.1007/s13399-022-03403-2.

[31] Y. Zhao, R. jie Tong, M.Q. Chen, F. Xia, Relative humidity sensor based on hollow core fiber filled with GQDs-PVA, Sensors Actuators, B Chem. 284 (2019) 96–102, https://doi.org/10.1016/j.snb.2018.12.130.

[32] H. Moustafa, A.M. Karmalawi, A.M. Youssef, Development of dapsone-capped TiO2 hybrid nanocomposites and their effects on the UV radiation, mechanical, thermal properties and antibacterial activity of PVA bionanocomposites, Environ. Nanotechnol. Monit. Manag. 16 (2021), 100482, https://doi.org/10.1016/j.enmm.2021.100482.

[33] K. Vidyalakshmi, K.N. Rashmi, T.M.P. Kumar, Siddaramaiah, Studies on formulation and in vitro evaluation of PVA/chitosan blend films for drug delivery, J. Macromol. Sci. Pure Appl. Chem. 41 A (2004) 1115–1122, https://doi.org/10.1081/MA-200026554.

[34] S. Ceylan, B. Alatepeli, Evaluation of PVA/Chitosan cryogels as potential tissue engineering scaffolds; synthesis, cytotoxicity, and genotoxicity investigations, J. Turkish Chem. Soc. Sect. A Chem. 8 (2021) 69–78, https://doi.org/10.18596/jotcsa.825115.

[35] W.C. Hsieh, J.J. Liau, Cell culture and characterization of cross-linked poly(vinyl alcohol)-g-starch 3D scaffold for tissue engineering, Carbohydr. Polym. 98 (2013) 574–580, https://doi.org/10.1016/j.carbpol.2013.06.020.

[36] E.M. Ahmed, H. Isawi, M. Morsy, M.H. Hemida, H. Moustafa, Effective nanomembranes from chitosan /PVA blend decorated graphene oxide with gum rosin and silver nanoparticles for removal of heavy metals and microbes from

water resources, Surfaces Interfaces 39 (2023), 102980, https://doi.org/10.1016/j.surfin.2023.102980.
[37] Hesham Moustafa, Nabila A. Darwish, Ahmed M. Youssef, Sameh M. Reda, Abd El-Aziz A. El-Wakill, High-performance of nanoparticles and their effects on the, Egypt. J. Chem. 21 (2018) 23–32.
[38] H. Moustafa, A.E.-A.A. El-Wakil, M.T. Nour, A.M. Youssef, Kenaf fibre treatment and its impact on the static, dynamic, hydrophobicity and barrier properties of sustainable polystyrene biocomposites, RSC Adv. 10 (2020) 29296–29305, https://doi.org/10.1039/D0RA05334A.
[39] ASTM, ASTM E104 Standard Practice for Maintaining Constant Relative Humidity by Means of, 02 (2014) 1–5.
[40] H. Moustafa, E.M. Ahmed, M. Morsy, Bio-based antibacterial packaging from decorated bagasse papers with natural rosin and synthesised GO-Ag nanoparticles, Mater. Technol. 37 (2022) 2766–2776, https://doi.org/10.1080/10667857.2022.2074939.
[41] H. Moustafa, H. Isawi, S.M.A. El, Environmental nanotechnology, monitoring & management utilization of PVA nano-membrane based synthesized magnetic GO-Ni-Fe 2 O 4 nanoparticles for removal of heavy metals from water resources, Environ. Nanotechnol. Monit. Manag. 18 (2022), 100696, https://doi.org/10.1016/j.enmm.2022.100696.
[42] F.T. Johra, J.W. Lee, W.G. Jung, Facile and safe graphene preparation on solution based platform, J. Ind. Eng. Chem. 20 (2014) 2883–2887, https://doi.org/10.1016/j.jiec.2013.11.022.
[43] U. Ruman, K. Buskaran, G. Pastorin, M.J. Masarudin, S. Fakurazi, M.Z. Hussein, Synthesis and characterization of chitosan-based nanodelivery systems to enhance the anticancer effect of sorafenib drug in hepatocellular carcinoma and colorectal adenocarcinoma cells, Nanomaterials 11 (2021) 1–28, https://doi.org/10.3390/nano11020497.
[44] J. Brzeska, A. Maria, E. Id, M. Morawska, W. Sikorska, M. Kowalczuk, M. Rutkowska, Branched Polyurethanes Based on Synthetic Polyhydroxybutyrate with Tunable Structure and Properties, (n.d.) 1–12. doi:10.3390/polym10080826.
[45] M.H. Buraidah, A.K. Arof, Characterization of chitosan/PVA blended electrolyte doped with NH 4I, J. Non. Cryst. Solids. 357 (2011) 3261–3266, https://doi.org/10.1016/j.jnoncrysol.2011.05.021.
[46] S. Chandra Dey, M. Al Amin, T. Ur Rashid, M. Zakir Sultan, M. Ashaduzzaman, M. Sarker, S. Md Shamsuddin, Preparation, characterization and performance evaluation of chitosan as an adsorbent for remazol red, Int. J. Latest Res. Eng. Technol. (2016) 52–62.
[47] M.R. Waikar, P.M. Raste, R.K. Sonker, V. Gupta, M. Tomar, M.D. Shirsat, R. G. Sonkawade, Enhancement in NH3 sensing performance of ZnO thin-film via gamma-irradiation, J. Alloys Compd. 830 (2020), 154641, https://doi.org/10.1016/j.jallcom.2020.154641.
[48] M.R. Waikar, R.K. Sonker, S. Gupta, S.K. Chakarvarti, R.G. Sonkawade, Post-γ -irradiation effects on structural, optical and morphological properties of chemical vapour deposited MWCNTs, Mater. Sci. Semicond. Process. 110 (2020), 104975, https://doi.org/10.1016/j.mssp.2020.104975.
[49] M. Morsy, I. Gomaa, M.M. Mokhtar, H. Elhaes, M. Ibrahim, Design and implementation of humidity sensor based on carbon nitride modified with graphene quantum dots, Sci. Rep. (2023) 1–18, https://doi.org/10.1038/s41598-023-29960-8.
[50] P. Ezati, A. Khan, J. Rhim, J. Tae, R. Molaei, Colloids and Surfaces B : biointerfaces pH-Responsive strips integrated with resazurin and carbon dots for monitoring shrimp freshness, Colloids Surfaces B Biointerfaces 221 (2023), 113013, https://doi.org/10.1016/j.colsurfb.2022.113013.
[51] E.L. Albert, C.A. Che Abdullah, Y. Shiroshaki, Synthesis and characterization of graphene oxide functionalized with magnetic nanoparticle via simple emulsion method, Results Phys. 11 (2018) 944–950, https://doi.org/10.1016/j.rinp.2018.10.054.
[52] L. Cao, F. Zhang, Q. Wang, X. Wu, Fabrication of chitosan/graphene oxide polymer nanofiber and its biocompatibility for cartilage tissue engineering, Mater. Sci. Eng. C. 79 (2017) 697–701, https://doi.org/10.1016/j.msec.2017.05.056.
[53] R. Panchal, T. Mateti, K. Likhith, F. Concy, G. Thakur, Genipin cross-linked chitosan – PVA composite films : an investigation on the impact of cross-linking on accelerating wound healing, React. Funct. Polym. 178 (2022), 105339, https://doi.org/10.1016/j.reactfunctpolym.2022.105339.
[54] H. Moustafa, S. Duquesne, B. Haidar, M.F.F. Vallat, Influence of the degree of exfoliation of an organoclay on the flame-retardant properties of cross-linked ethylene-co-Propylene-co-diene monomer-g-Maleic anhydride-based composites, Polym. Compos. 38 (2017) 966–973, https://doi.org/10.1002/pc.23659.
[55] M. Morsy, M. Ibrahim, Z. Yuan, F. Meng, Graphene foam decorated with ZnO as a humidity sensor, IEEE Sens. J. (2020) 20, https://doi.org/10.1109/JSEN.2019.2948983.
[56] E. Ouda, Flexible humidity sensor based on light-scribed graphene oxide, J. Mater. Sci. Mater. Electron. (2022), https://doi.org/10.1007/s10854-022-08681-0.
[57] M. Morsy, M.M. Mokhtar, S.H. Ismail, G.G. Mohamed, M. Ibrahim, Humidity sensing behaviour of lyophilized rGO/Fe2O3 nanocomposite, J. Inorg. Organomet. Polym. Mater. 30 (2020) 4180–4190, https://doi.org/10.1007/s10904-020-01570-1.
[58] K. Mistewicz, A. Starczewska, M. Jesionek, M. Nowak, M. Kozioł, D. Stróż, Humidity dependent impedance characteristics of SbSeI nanowires, Appl. Surf. Sci. (2020) 513, https://doi.org/10.1016/j.apsusc.2020.145859.
[59] M. Jesionek, B. Toroń, P. Szperlich, W. Biniaś, D. Biniaś, S. Rabiej, A. Starczewska, M. Nowak, M. Kępińska, J. Dec, Fabrication of a new PVDF/SbSI nanowire composite for smart wearable textile, Polymer (Guildf) 180 (2019), 121729, https://doi.org/10.1016/j.polymer.2019.121729.
[60] W.M. Taha, M. Morsy, N.A. Nada, M. Ibrahim, Diamond & related materials studying the humidity sensing behavior of MWCNTs boosted with Co 3 O 4 nanorods, Diam. Relat. Mater. 121 (2022), 108754, https://doi.org/10.1016/j.diamond.2021.108754.
[61] R.K. Sonker, B.C. Yadav, Growth mechanism of hexagonal ZnO nanocrystals and their sensing application, Mater. Lett. 160 (2015) 581–584, https://doi.org/10.1016/j.matlet.2015.06.090.
[62] M. Morsy, A.I. Abdel-Salam, M. Mostafa, A. Elzwawy, Promoting the humidity sensing capabilities of titania nanorods/rGO nanocomposite via de-bundling and maximizing porosity and surface area through lyophilization, Micro Nano Eng. 17 (2022), 100163, https://doi.org/10.1016/j.mne.2022.100163.
[63] A. Beniwal, P. Ganguly, A.K. Aliyana, G. Khandelwal, R. Dahiya, Screen-printed graphene-carbon ink based disposable humidity sensor with wireless communication, Sensors Actuators B Chem. 374 (2023), 132731, https://doi.org/10.1016/j.snb.2022.132731.
[64] B. Priyadharshini, P. Valsalal, An improved humidity sensor with GO-Mn-Doped ZnO nanocomposite and dimensional orchestration of comb electrode for effective bulk manufacturing, Nanomaterials (2022) 12, https://doi.org/10.3390/nano12101659.
[65] D. Zhang, J. Tong, B. Xia, Humidity-sensing properties of chemically reduced graphene oxide/polymer nanocomposite film sensor based on layer-by-layer nano self-assembly, Sensors Actuators B Chem. 197 (2014) 66–72, https://doi.org/10.1016/j.snb.2014.02.078.
[66] A.M.Soomro Zeeshan, S. Cho, Design and fabrication of a robust chitosan/polyvinyl alcohol-based humidity sensor energized by a piezoelectric generator, Energies (2022) 15, https://doi.org/10.3390/en15207609.
[67] Y. Guo, H. Xi, Z. Gu, M. Li, X. Li, D. Gao, A self-powered PVA-based flexible humidity sensor with humidity-related voltage output for multifunctional applications, Colloids Surfaces A Physicochem. Eng. Asp. 658 (2023), 130700, https://doi.org/10.1016/j.colsurfa.2022.130700.
[68] S.A. Rahman, S.A. Khan, M.M. Rehman, W.Y. Kim, Highly sensitive and stable humidity sensor based on the Bi-layered PVA/graphene flower composite film, Nanomaterials (2022) 12, https://doi.org/10.3390/nano12061026.
[69] S. Kumar, C.S. Kushwaha, P. Singh, K. Kanojia, S.K. Shukla, Chemiresistive sensor for breath frequency and ammonia concentration in exhaled gas over a PVA/PANI/CC composite film, Sensors Diagnostics (2023), https://doi.org/10.1039/D3SD00067B.
[70] Y. Huan, Q. Kong, H. Mou, H. Yi, Antimicrobial peptides: classification, design, application and research progress in multiple fields, Front. Microbiol. 11 (2020) 1–21, https://doi.org/10.3389/fmicb.2020.582779.
[71] F. Sha, Z. Aftab, H. Ra, G. Li, Green synthesis and application of GO nanoparticles to augment growth parameters and yield in mungbean (Vigna radiata L .), (2022) 1–19. doi:10.3389/fpls.2022.1040037.